Tellus (2000), 52A, 140–161
Printed in UK. All rights reserved

TELLUS
ISSN 0280–6495

Atmospheric water species budget in mesoscale simulations of lee cyclones over the Mackenzie River Basin

By VASUBANDHU MISRA*, M. K. YAU and NAGARAJAN BADRINATH, *Department of Atmospheric and Oceanic Sciences, McGill University, Montreal, Quebec H3A2K6, Canada*

(Manuscript received 11 January 1999; in final form 30 September 1999)

ABSTRACT

A moisture budget over the Mackenzie River Basin (MRB) was computed using a high-resolution mesoscale model with explicit microphysics for 3 lee cyclogenesis events. A unique feature of the calculation is that all the budget terms are calculated from the model and no residual terms are required. It was found that during the initial formative period of the lee cyclones, a large influx of moisture occurs at the western boundary. However, as the cyclone moves further east, a significant amount of moisture is withdrawn through the eastern and southern boundaries of the basin. Surface evaporation was found to be relatively large during the local day time and plays a vital rôle in initiating convection in the presence of frontal lifting south of 60°N within the basin. In 2 of the 3 cases, the total water in the basin increases over the history of the simulation as a result of substantial lateral flux convergence of total water content even though the total precipitation in these two events was nearly 1.4× the surface evaporation. For the 3rd cyclone, the total water in the basin decreases substantially because of precipitation and large outward moisture flux at the boundary. The dominant microphysical processes governing the transformation of various water species were condensation, deposition, autoconversion and accretion of cloud water by rain, accretion of cloud water by ice, melting of ice to rain water and evaporation of cloud and rain water. In the net horizontal flux convergence of water species, the largest was water vapor, followed by ice and cloud water. The net flux convergence of rainwater into the basin was small and the effect of the graupel processes is negligible.

1. Introduction

The World Climate Research Program (WCRP) initiated the Global Energy and Water Cycle Experiment (GEWEX) to understand the rôle of energy and water cycle in the global climate system. The Mackenzie River Basin (MRB; see Fig. 2 (or 9)) is one of the 5 sites chosen for the continental scale experiment. This site is important in understanding the effect of hydrological and meteorological processes in high latitude cold regions on the global climate.

* Corresponding author.
e-mail: misra@zephyr.meteo.mcgill.ca

The basin is however, covered very poorly by observations. There are only 14 surface stations (Lackmann and Gyakum, 1996) and 6 upper air stations (Walsh et al., 1994). Therefore, our strategy is to use the output data from a non-hydrostatic model, which are continuous in time and space and are dynamically consistent, to determine the water budget and important physical processes in major precipitating systems over the area. Our budget calculation is novel in 2 aspects. First the water cycle in this study includes explicitly several different forms of atmosphere water, and not just water vapor. This is accomplished through the computation of the mixing ratios of water vapour (q_v), cloud water (q_c), rain

water (q_r), ice (q_i) and graupel (q_g) in high-resolution simulations of lee cyclones using the Mesoscale Compressible Community (MC2) model. Second, unlike most budget studies (Smirnov and Moore, 1999) where post-processed data were used to determine one of the budget terms as a residue, we computed directly all the terms of the budget at each time step in the model and no residual calculation is required. Earlier studies (Kong and Yau, 1997; Lackmann et al., 1998; Benoit et al., 1997) have indicated that MC2 demonstrates a high skill in simulating extra-tropical systems. This fact is exploited in quantifying the effects of the various forcings in the equations governing q_v, q_c, q_r, q_i and q_g.

Past studies indicate that the moisture transport over the MRB reaches a maximum during frequent cyclonic activity (Bjornsson et al., 1995; Walsh et al., 1994). Lackmann and Gyakum (1996) used 28 years of gridded sea level pressure data from NCEP (National Center for Environment Prediction) to classify precipitating weather systems over the basin into three categories — lee cyclones, interior cyclones which have no antecedents in the Gulf of Alaska and intense Arctic anticyclones in the northern part of the basin. They found from their composite study on lee cyclogenesis that the wetter lee cyclones over the MRB are coincident with strong southwesterly perturbation geostrophic flow pattern.

In this study, we chose 3 lee cyclogenesis events observed during the Beaufort and Arctic Storms Experiment (BASE) conducted between 1 September and 15 October 1994. Our strongest case (hereafter case N) occurred between 06.00 UTC, 24 September to 18.00 UTC, 26 September. It made its passage through the northern part of the basin. Another event (hereafter case S) commenced on 00.00 UTC, 14 September and lasted till 12.00 UTC, 16 September. This storm traversed the southern section of the basin and was less intense than case N. The third episode (hereafter case C) was observed between 00.00 UTC, 18 September and 00.00 UTC, 19 September and tracked through the central portion of the MRB. A pilot 36-h integration was first performed for the three cases at a coarser resolution of 50 km (true at 60°N on a polar stereographic projection) using initial and boundary conditions from the Canadian Meteorological Center (CMC) analysis. This was followed by the higher resolution 18 km simulation using initial conditions and boundary conditions updated every 6 hours from the 50-km run. Table 1 contains a summary of the 3 cases.

A brief description of the model is presented in the following section. The methodology adopted is given in Section 3. Section 4 discusses the results followed by conclusions in Section 5.

2. A brief outline of the MC2 model

The MC2 model is a non-hydrostatic model based on the Navier-Stokes equations (Benoit et al., 1997). It utilizes the terrain following Gal-Chen coordinate system on a polar stereographic projection. The prognostic variables are u, v, w, $\ln(p/p_o)$, T, q_v, q_c, q_r, q_i and q_g, where p_o is a reference pressure of 1000 hPa. The numerical method used is the semi-implicit semi-Lagrangian scheme.

The model has a comprehensive physics package. It includes planetary boundary layer processes based on turbulent kinetic energy (Benoit et al., 1989), implicit vertical diffusion, and a surface layer scheme using similarity theory. The surface temperature over land is predicted via the force restore method (Deardorff, 1978; Benoit et al., 1989). The diurnal cycle associated with solar and infrared fluxes over ground is modulated by diagnostic clouds. The solar and infrared schemes in the radiation package of the model are fully interactive with the clouds (Garand and Mailhot, 1990). The total precipitation is the sum of the convective and stratiform precipitation. The former is generated by a Kuo type deep cumulus parameterization implemented by Mailhot and Chouinard (1989). An explicit microphysics scheme (Kong and Yau, 1997; Kong et al., 1990) produces the stratiform precipitation.

For the 18 km run, the total number of grid points in the horizontal and vertical directions is $160 \times 180 \times 25$. The model lid is at 25 km. The vertical grid length is not uniform and the thermodynamic variables are placed at 80, 240, 420, 630, 865, 1135, 1440, 1790, 2190, 2640, 3155, 3740, 4410, 5170, 6035, 7025, 8145, 9425, 10885, 12545, 14430, 16585, 19035 and 21825 m in the Gal Chen coordinate. The time step is 2 min.

Table 1. *Outline of the experiments conducted*

Name of expt.	At 50 km resolution		At 18 km resolution		Location of lee cyclone w.r.t. center of the MRB
	start time	end time	start time	end time	
case N	24 Sept., 1200 UTC	26 Sept., 0000 UTC	25 Sept., 0000 UTC	26 Sept., 0000 UTC	north
case S	13 Sept., 1200 UTC	15 Sept., 0000 UTC	14 Sept., 0000 UTC	15 Sept., 0000 UTC	south
case C	17 Sept., 1200 UTC	19 Sept., 0000 UTC	18 Sept., 0000 UTC	19 Sept., 0000 UTC	center

3. Methodology

The model provides prognostic variables and forcing terms in high temporal and spatial resolutions yet maintains excellent mass conservation of water substances. The model can therefore be used to study the budgets of precipitation systems within a fixed area comprising the MRB. Similar methodology has been adopted over the tropics (Krishnamurti et al., 1996a, b).

To derive the budget equation for the jth water species with mixing ratio q_j over the MRB, we first write its continuity equation in Cartesian coordinate (x, y, z) as

$$\frac{\partial \rho q_j}{\partial t} + \nabla\cdot(\rho \boldsymbol{V} q_j) = \rho \dot{S}_j,$$

where ρ *is the air density,* $\dot{S}_j$ is the source and sink terms per unit mass of air, $\boldsymbol{V}$ is the 3-dimensional air velocity, and ∇ is the three-dimensional gradient operator.

In terms of the Gal-Chen coordinate ς, defined as

$$\varsigma = H\left[\frac{z - h_0(x, y)}{H - h_0(x, y)}\right], \tag{2}$$

with H being the top of the domain and h_0 the topography, (1) can be written as

$$\frac{\partial \rho q_j}{\partial t} + \nabla_\varsigma\cdot(\rho \boldsymbol{V} q_j) + \frac{\partial(\rho \boldsymbol{V} q_j)}{\partial \varsigma}\cdot\nabla\varsigma = \rho \dot{S}_j, \tag{3}$$

where is ∇_ς the gradient operator in Gal-Chen coordinate.

By integrating (3) from the surface ($\zeta = 0$) to the top of the domain ($\zeta = H$), and using the boundary conditions $\boldsymbol{V} = 0$ at $\zeta = 0$ and $q_j = 0$ at $\zeta = H$, it can be shown that

$$\frac{\partial}{\partial t}\int_0^H \partial q_j \, \mathrm{d}\varsigma + \int_0^H \nabla_H\cdot(\rho \boldsymbol{V}_H q_j)\mathrm{d}\varsigma = \int_0^H \rho \dot{S}_j \, \mathrm{d}\varsigma, \tag{4}$$

where $\boldsymbol{V}_H$ and ∇_H are the horizontal velocity and horizontal gradient operator respectively.

The budget equation for q_j in the whole volume over the MRB can be obtained by integrating (4) over the horizontal area of the MRB. By using (2) and the hydrostatic equation, and neglecting the small horizontal variation of $\partial\zeta/\partial z$, the horizontal integral of (4) becomes

$$\begin{aligned}\frac{\partial}{\partial t}\left[-\frac{1}{g}\int_{\mathrm{psurf}}^{\mathrm{ptop}}\iint_{\mathrm{MRB}} q_j \, \mathrm{d}x \, \mathrm{d}y \, \mathrm{d}p\right] \\ + \left[-\frac{1}{g}\oint_{\mathrm{MRB}}\left\{\int_{\mathrm{psurf}}^{\mathrm{ptop}} V_n q_j \, \mathrm{d}p\right\}\mathrm{d}l\right] \\ = -\frac{1}{g}\int_{\mathrm{psurf}}^{\mathrm{ptop}}\iint_{\mathrm{MRB}} \dot{S}_j \, \mathrm{d}x \, \mathrm{d}y \, \mathrm{d}p,\end{aligned} \tag{5}$$

where V_n is the horizontal wind normal to the boundary of the MRB, $\mathrm{d}l$ is the differential length along the perimeter of the MRB, and g is the acceleration due to gravity.

Eq. (5) shows that the time rate of change of the total mass of water species j in the whole air mass over the MRB (so-called the storage term) is given by the vertical integral of the horizontal flux convergence through the lateral boundaries and the total integral of the source and sink terms. Obviously, eq. (5) can also be applied over the whole domain of integration. In the absence of sources and sinks and horizontal flux divergence at the lateral boundaries of the domain, (5) shows

that the total mass of q_j in the domain,

$$-\frac{1}{g}\iiint_{\text{wholedomain}} q_j \, dx \, dy \, dp,$$

is invariant with time.

The values of q_j required in (5) is given by the solution of a prognostic equation. Specifically, the prognostic equations for the mixing ratios of the 5 water species are:

$$\frac{dq_v}{dt} = \text{AVD}_{\text{gv}} + \text{AMVD}_{\text{gv}} - \text{ANU}_{\text{vi}} + \text{AVD}_{\text{vi}} - \text{Cond.} + \text{CE} + \text{RE} - \text{CD} + \text{D} \quad (6)$$

$$\frac{dq_c}{dt} = \text{AML}_{\text{ic}} - \text{AHNU}_{\text{ci}} - \text{ACL}_{\text{ci}} - \text{ACL}_{\text{cg}} - \text{AC}_{\text{w}} + \text{Cond.} - \text{CE} \quad (7)$$

$$\frac{dq_r}{dt} = \text{AML}_{\text{gr}} - \text{ANU}_{\text{rg}} - \text{AHNU}_{\text{rg}} - \text{AFR}_{\text{rg}} - \text{ACL}_{\text{rg}} - \text{AMVD}_{\text{gv}} + \text{AC}_{\text{w}} - \text{RE} \quad (8)$$

$$+ \text{AML}_{\text{ir}} - \text{SQ}_{\text{r}}$$

$$\frac{dq_i}{dt} = \text{ANU}_{\text{vi}} + \text{AHNU}_{\text{ci}} + \text{AVD}_{\text{vi}} + \text{ACL}_{\text{ci}} + \text{AMUR}_{\text{gi}} + \text{AMUF}_{\text{gi}} - \text{AML}_{\text{ic}} - \text{ACN}_{\text{ig}} - \text{ACL}_{\text{ig}} - \text{AML}_{\text{ir}} - \text{SQ}_{\text{i}} \quad (9)$$

$$\frac{dq_g}{dt} = \text{ANU}_{\text{rg}} + \text{AHNU}_{\text{rg}} + \text{ACN}_{\text{ig}} + \text{AFR}_{\text{rg}} + \text{ACL}_{\text{cg}} + \text{ACL}_{\text{ig}} - \text{AVD}_{\text{gv}} - \text{AML}_{\text{gr}} - \text{AMUR}_{\text{gi}} - \text{AMUF}_{\text{gi}} + \text{ACL}_{\text{rg}} - \text{SQ}_{\text{g}} \quad (10)$$

The symbols on the right-hand side of (6)–(10) are explained in Section 7. The total water content ($q_v + q_c + q_r + q_i + q_g$) is only affected by the terms CD, D, SQ_{r}, SQ_{i} and SQ_{g}. Convective drying (CD) is associated with the cumulus parameterization scheme. When convection occurs, convective precipitation forms and falls to the ground. Water vapor is extracted from the atmosphere to provide for the convective precipitation. The symbols D, SQ_{r}, SQ_{i}, and SQ_{g} denote the vertical divergence of turbulent moisture flux and the sedimentation terms for rain, ice, and graupel (vertical divergence of precipitation flux) respectively. When integrated vertically, they yield the surface evaporation rate and the surface stratiform precipitation rates. The remaining symbols represent microphysical conversation processes between different water species. A detailed derivation of these terms are in Kong and Yau (1997) and Kong et al. (1990). Fig. 1 illustrates schematically the basic working of the microphysics in MC2.

A two step procedure is used to obtain the solution for (6)–(10). First, the semi-Lagrangian advection scheme is used to obtain the value of q_j at a grid point. Then the source and sink terms are calculated and the value of q_j adjusted to complete the solution for one time step. Because semi-Lagrangian advection is not completely mass conserving, it becomes important to determine the degree of conservation of the total mass of qj in the integration domain. Experiments show that for the three cases under consideration, the MC2 model conserves very well the total mass of water vapour in the whole domain at each time step after advection. For the less continuous fields like q_c, q_r, q_i and q_g, with the boundary condition that $q_c = q_r = q_i = q_g = 0$ at the lateral boundaries of our large domain, the total mass of these hydrometeors should be exactly conserved before the adjustment for the source and sink terms. Therefore, to ensure exact conservation of the hydrometeors in the runs presented here, we multiplied q_c, q_r, q_i and q_g at every time step after the semi-Lagrangian advection by the ratio $\Sigma\Sigma\Sigma q_j^{n-1}\Delta p_k^{n-1} / \Sigma\Sigma\Sigma q_j^{n+1}\Delta p_k^{n+1}$, where $\Sigma\Sigma\Sigma q_j^{n-1}\Delta p_k^{n-1}/g$ is the total mass of water species q_j in the domain at time step $(n-1)$ and $\Sigma\Sigma\Sigma q_j^{n+1}\Delta p_k^{n+1}/g$ is the total mass of q_j in the whole domain at the time step $(n+1)$ after advection. No correction was applied to q_v. These corrections did not alter the simulated fields in any perceptible manner.

4. Results

4.1. Model forecast verification

In this Subsection, the synoptic validation of the higher resolution simulation is presented. The vapor budget, horizontal moisture flux convergence into the basin and the role of microphysics are delineated in subsequent subsections. To avoid errors from interpolation, all budgets were computed on model Gal-Chen levels on the Arakawa-C grid.

The model simulated lee cyclogenesis successfully in all three cases. Fig. 2 shows the mean sea

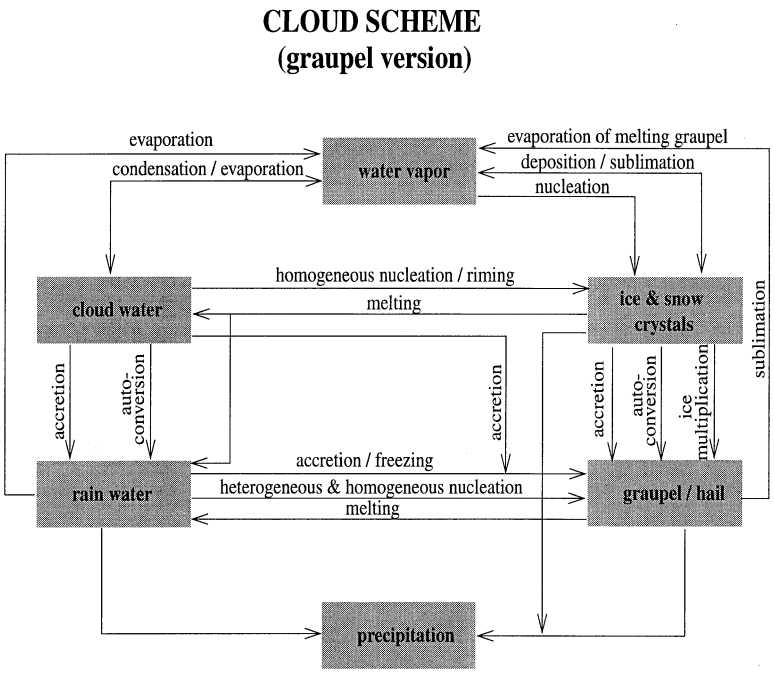

Fig. 1. A schematic diagram of the microphysics in MC2. The boxes indicate the various water species. The arrows denote the direction of mass transfer.

level pressure (MSLP) and the 850-hPa temperature at 00.00 UTC (24 h into the integration). In case N (Fig. 2a), the parent cyclone in the Gulf of Alaska dissipated into a trough and a lee cyclone forms in the northern part of the MRB. In contrast, in cases S (Fig. 2b) and C (Fig. 2c), the parent cyclone continues to remain in the Gulf of Alaska during the genesis and decay of the lee cyclones. Figure 3 exhibits the MSLP analysis and the location of the surface fronts at the same time. The position of the cyclones, their central pressure and pressure gradients are similar between the simulation and analysis. The tight 850-hPa temperature gradients are aligned with the analyzed surface frontal positions (compare Figs. 2, 3). Despite the paucity of observations over the MRB, the model has considerable skill in simulating the cyclones.

Fig. 4 shows the accumulated total precipitation over the history of the simulation for the three cases. We excluded the precipitation for the first 3 hours to minimize the effect of spin-up. In large part, stratiform precipitation generated by the explicit microphysics scheme occurs towards the eastern side of the basin. Convective precipitation associated with the cumulus parameterization was mostly confined to regions of steep orography near the western boundary of the basin. In cases N and S, the model simulated some convective precipitation to the south of 60°N. This convective rainfall is partly related to the diurnal variation in surface evaporation and we will discuss it in more detail later. A distinct area of rain shadow on the lee side of the Mackenzie mountains is evident. The rain shadow is associated with the downslope flow induced by the orography.

4.2. *Vapor budget*

4.2.1. Case N. This case was the most intense of the three. Fig. 5 illustrates the time series of various components of the water vapor budget equation obtained by setting $q_j = q_v$ in (5). Each data point represents an average over 10 timesteps (20 min) in units of megaton/h (1 megaton = 10^9 kg). The storage term of q_v (Tend. of q_v) closely follows the net horizontal moisture flux convergence (Conv. Hor. Flux) into the basin and is positive during the initial 15 h (450 time steps).

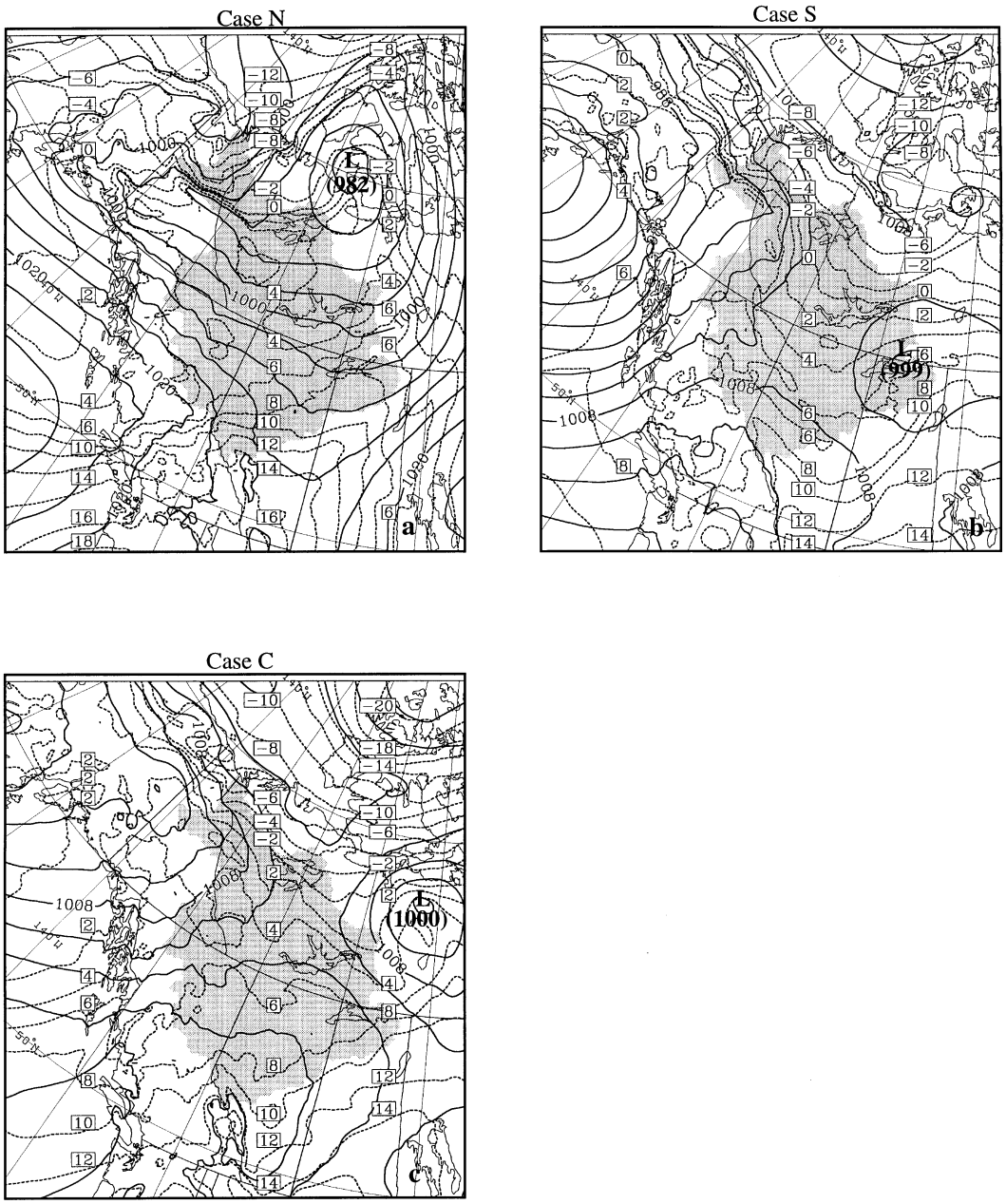

Fig. 2. Simulated mean sea level pressure (contour interval 4hPa, solid) overlaid with 850 hPa isotherms (contour inteval 2°C, dashed) valid at a) 00.00 UTC 26 Sept, b) 00.00 UTC 15 Sept and c) 00.00 UTC 19 Sept. The shaded area represents the Mackenzie River Basin.

The sign reverses in the next 9 h as the storm moves out of the MRB and the basin becomes drier. The other source and sink terms represent the rate of microphysical processes in the total mass of air over the basin. Although their magnitudes are much smaller, they ultimately determine the difference between the storage and the net flux convergence into the MRB. It is evident that

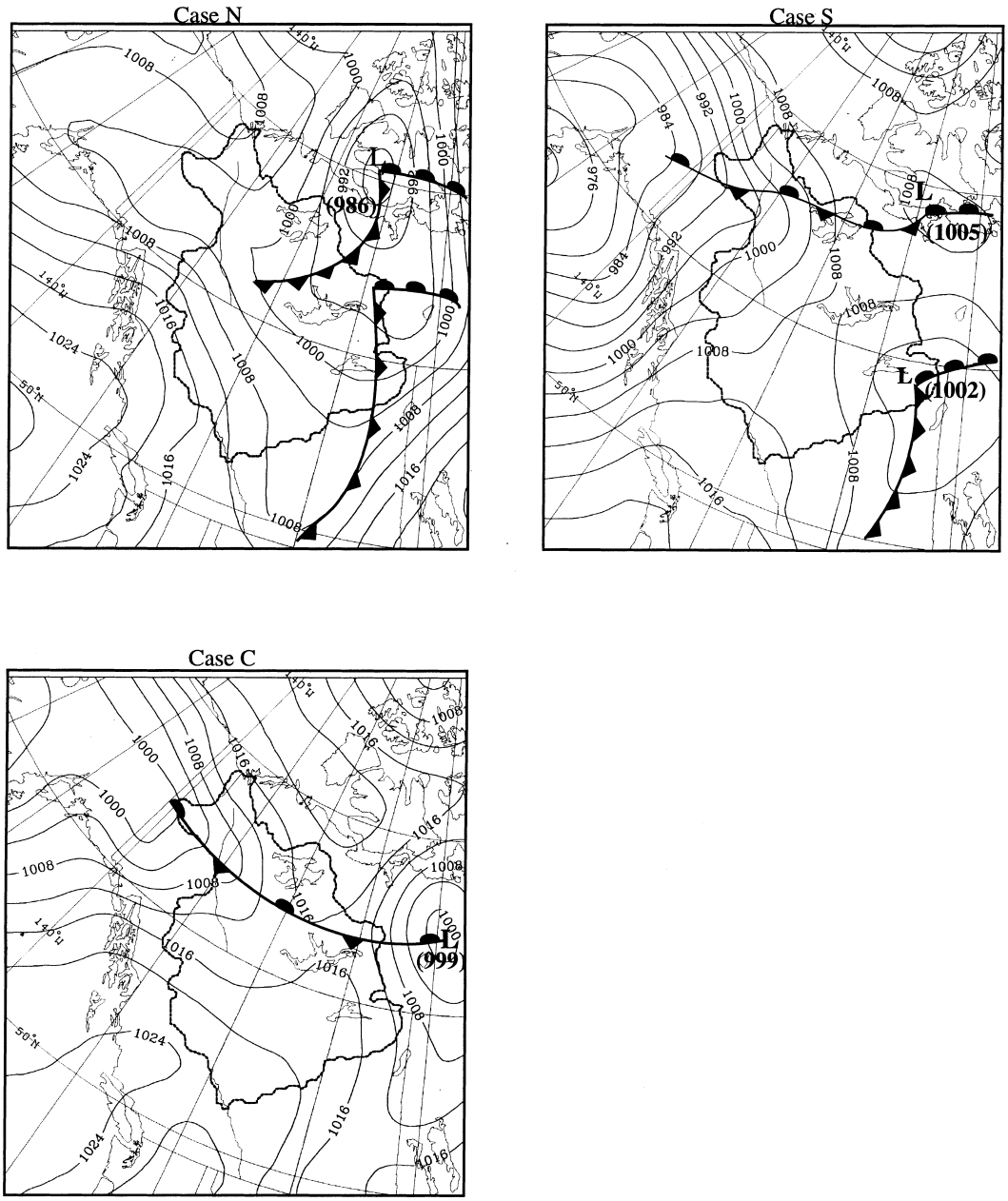

Fig. 3. The mean sea level pressure from Canadian Meteorological Center analysis overlaid with surface fronts valid at (a) 00.00 UTC 26 Sept, (b) 00.00 UTC 15 Sept and (c) 00.00 UTC 19 Sept. The contour interval is 4hPa.

deposition (AVD_{vi}), condensation (Cloud cond.), evaporation of cloud water (Cloud evap), and evaporation of rain water (Rain evap) are the dominant microphysical forcings acting on q_v. In addition, the area integrated surface evaporation (Sfc. Evap.) and convective drying over the basin show significant amplitude in the afternoon during the latter part of the simulation.

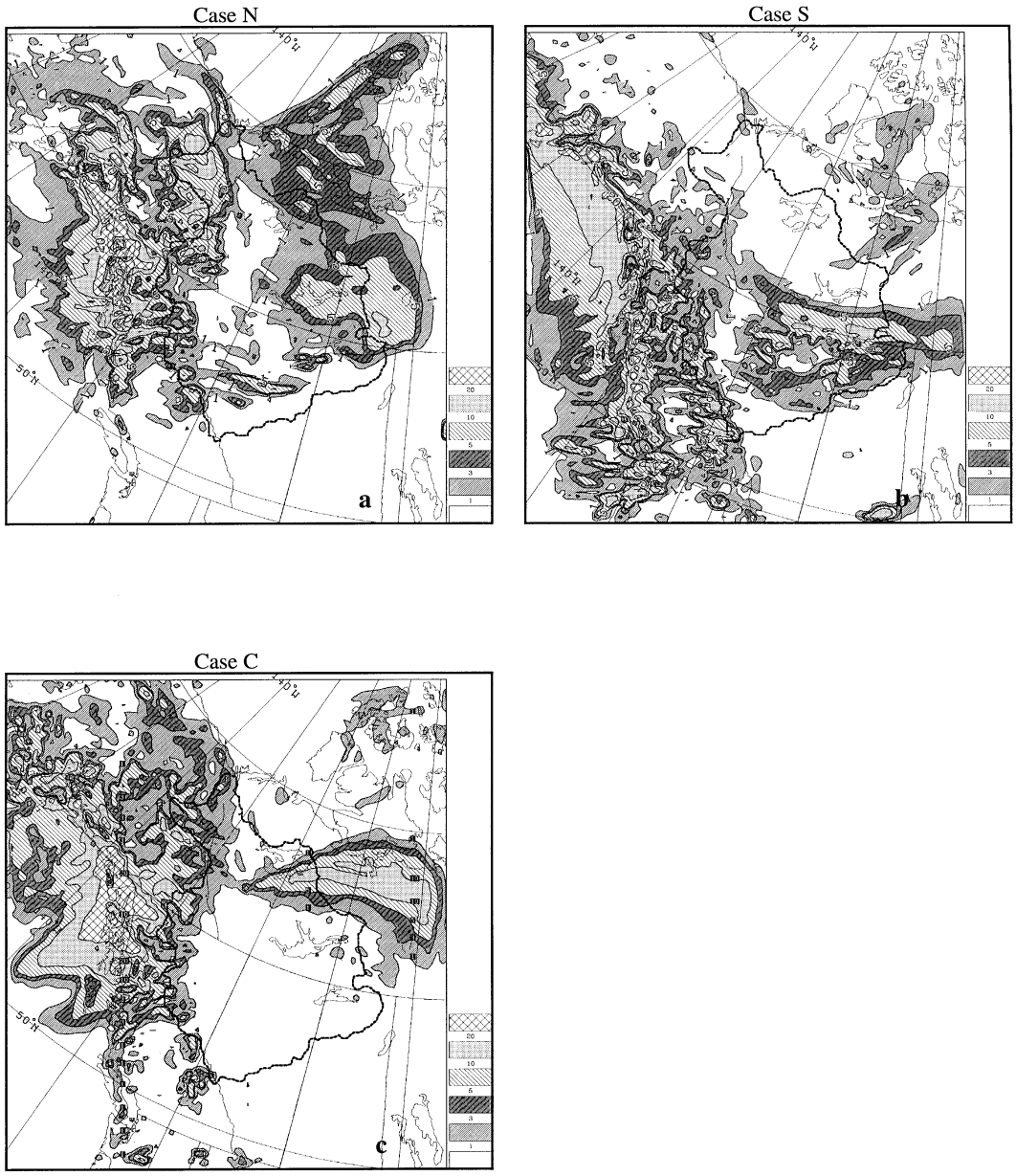

Fig. 4. 21-h total accumulated precipitation in mm for (a) case N (03.00 UTC 25 Sept-00.00 UTC 26 Sept), (b) case S (03.00 UTC 14 Sept-00.00 UTC 15 Sept) and (c) case C (03.00 UTC 18 Sept-00.00 UTC 19 Sept).

4.2.2. Case S. This case was less intense than case N. The vapour budget (Fig. 6) is dominated by the net horizontal flux convergence during the first 12 h (360 timesteps). Thereafter, surface evaporation and convective drying predominate. Deposition (AVDvi), condensation (Cloud Cond.), evaporation of cloud water (Cloud evap) and evaporation of rain water (Rain evap) are again the dominant microphysical forcing terms.

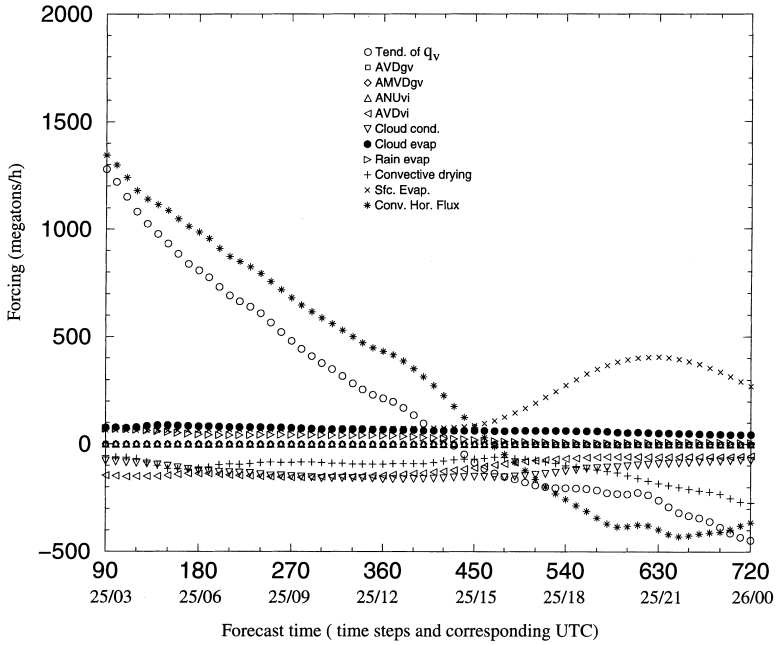

Fig. 5. The time series of vapor budget for case N. The abscissa denotes the number of time steps and the corresponding date and time in UTC. The ordinate denotes the magnitude of the forcing in units of megatons/h.

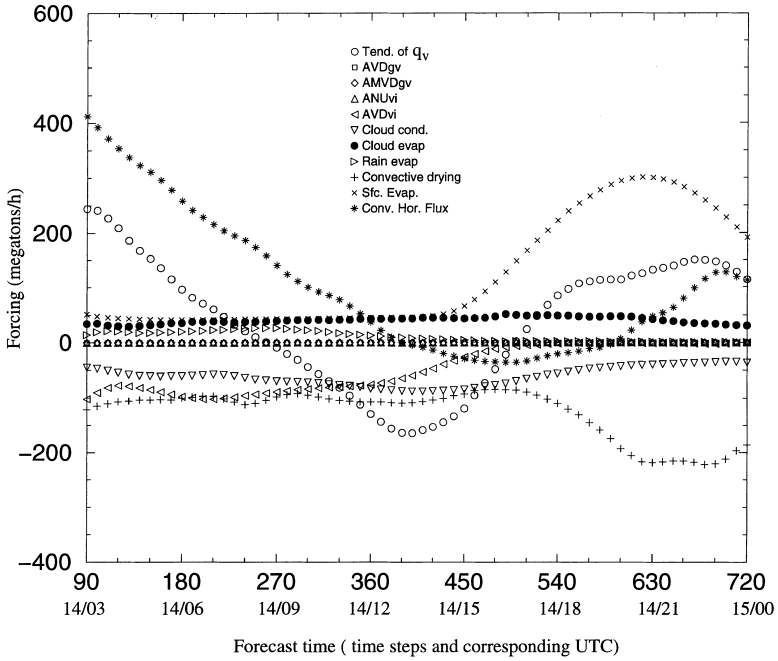

Fig. 6. Same as Fig. 5 but for case S.

4.2.3. Case C. The storage of vapour in the basin is strongly dictated by the net horizontal flux convergence even in case C (Fig. 7). For most part the net moisture flux is diverging and the magnitude of the other forcings is relatively small. Surface evaporation again increases during the day but the increase in convective drying is not as large as in the other 2 cases. The reason is that the storm is relatively weak and its passage is not in phase with the diurnal variation of the surface evaporation.

To sum up, the net horizontal flux convergence predominates the water vapour budget during the period of lee cyclogenesis. For the 3 cases studied, this feature was found independent of the location of the cyclone in the MRB. The simulations also show a diurnal cycle in the surface evaporation whose importance is further examined below.

4.3. The rôle of surface evaporation

Surface evaporation strongly influences the total water vapour budget particularly during the last 6 h of the simulations. Fig. 8a shows the predicted surface moisture flux (or surface evaporation) for case N at 18.00 UTC (local noon) when the fluxes increase to >200 Wm^{-2} in the southern portion of the basin. A similar behavior is indicated in case C (Fig. 8b) and case S (not shown). A comparison with the 7-h (15.00UTC–22.00UTC) accumulated convective precipitation (Fig. 8c, d) reveals that for case N, regions of significant convection in the afternoon coincide with areas of high surface evaporation. The same situation, however, did not occur in case C because regions of large surface evaporation in the basin did not overlap with the position of the surface front. As a result, the maximum convective drying in the basin for case N and case S are respectively 285 and 200 megatons/h whereas it is less than 100 megatons/h for case C.

We conducted a sensitivity experiment by suppressing surface evaporation over land for the northern storm. In this case convection did not occur in the basin south of 60N or east of 120W despite relatively strong temperature gradient near the surface. Thus, one may surmise that the increase in convective drying and convective precipitation in the latter part of the simulation results from a combination of surface evaporation and surface frontal forcing.

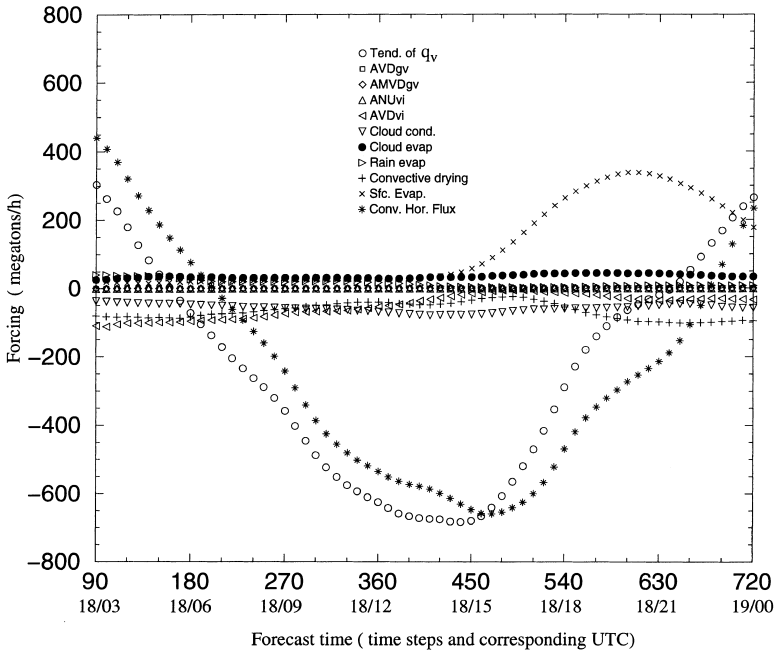

Fig. 7. Same as Fig. 5 but for case C.

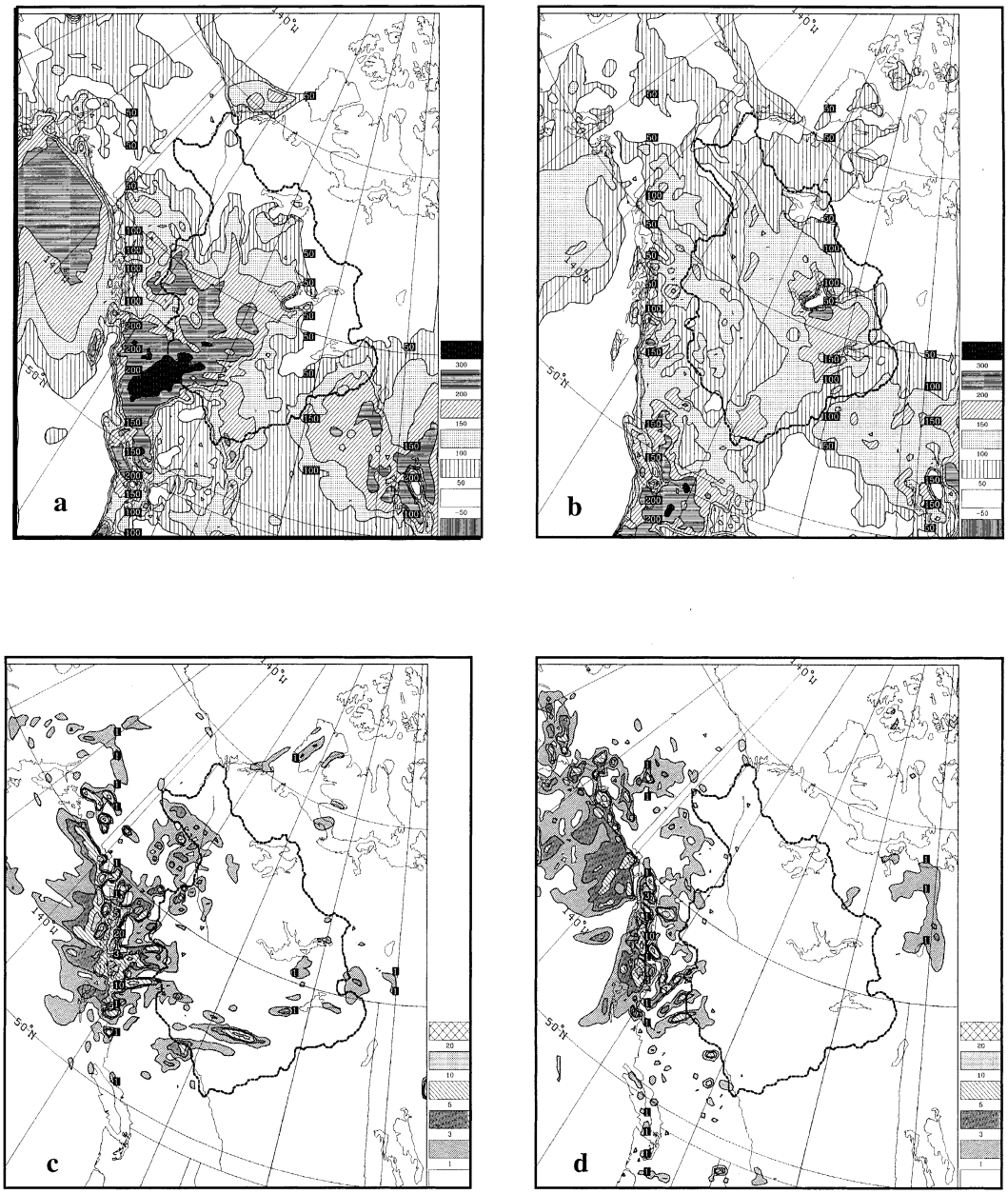

Fig. 8. The simulated surface moisture flux (Wm^{-2}) at (a) 18.00 UTC 25 Sept for case N and (b) 18.00 UTC 18 Sept for case S. The simulated 7-h accumulation of convective precipitation (c) between 15.00–22.00 UTC 25 Sept for case N and (d) between 15.00–22.00 UTC 18 Sept for case C.

4.4. *The horizontal water vapour flux across different sectors*

Having shown that the net horizontal moisture flux convergence is the largest forcing in the vapor budget, we further divided the basin into four quadrants (Fig. 9) and computed the horizontal fluxes across four sectors from 03.00 UTC to 24.00 UTC. Specifically, we calculated the line integral of $V_n q_v$ along the path length of the sectors. For clarity of presentation, sectors 1, 2, 3 and 4 will be referred to as the southwest (SW), southeast (SE), northeast (NE), and northwest (NW) sector, respectively.

4.4.1. Case N. Fig. 10a shows substantial net moisture flux into the basin through the SW sector and net outward flux through the NE sector throughout the 21-h period. The net flux through the SE sector is also outward, but it only grows to a nonnegligible magnitude towards the end of the period. The net moisture inflow through the NW sector likewise increases with time. An examination of the low-level wind (not shown) indicates that a significant portion of the net moisture inflow through the NW sector comes from the Beaufort Sea. A time height cross-sections shows strong low to mid tropospheric inward flux from the southwest (Fig. 11a) and a corresponding outward flux at an altitude around 2640 m through the NE sector (Fig. 11c). The outward flux increases as the cyclone moves eastward and it reaches its peak value at about 18 h of simulation time. The SE sector (Fig. 11b) depicts decreasing low-level inward flux and increasing mid-tropospheric outward flux; a behaviour consistent with the eastward movement of the large scale low level trough and upper level ridge. The NW sector (Fig. 11d) exhibits increasing large flux convergence at around 865 m altitude. The northern track of the lee cyclone results in the vertically integrated flux through the SE sector being an order of magnitude smaller than the other three sectors.

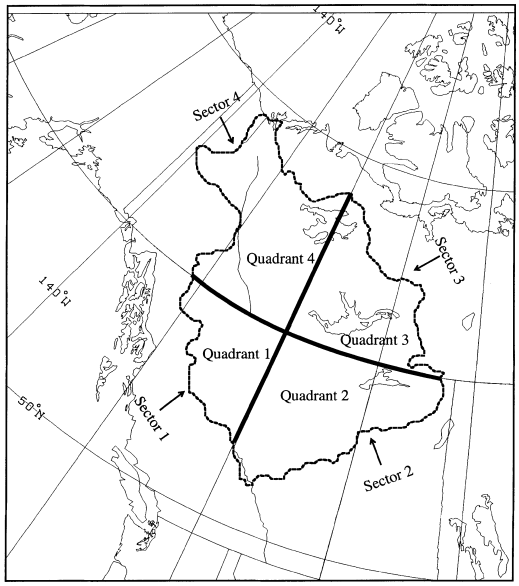

Fig. 9. The four quadrants and sectors of the MRB. Refer to the text for details.

4.4.2. Case S. This cyclone is weaker than case N and the moisture flux smaller (Fig. 10b). In contrast to the northern cyclone, the largest net outward flux appears in the SE sector instead of the NE sector. Inward flux again appears in the SW sector and the time height section (not shown) indicates its maximum amplitude at around 1440 m (700 hPa). Relatively small inward moisture fluxes through the depth of the lower troposphere are found in the NW sector.

4.4.3. Case C. Unlike the previous 2 cases, this cyclone exhibited a net divergence of moisture flux from the basin. Large negative flux appears in the SE and NE sectors (Fig. 10c) while net positive flux is associated with the sectors NW and SW. The surge of moisture through the southwest boundary extends from the surface to about 4400 m (not shown). The largest outward flux through the NE sector appears around 3.5 km.

In all the three cyclones studied, the net moisture fluxes through the NW and SW sectors are always inward. The fluxes through the NE and SE sectors are generally outward, but this outflow is smaller in the 2 cyclones that passed through the northern and southern extremes of the basin than in the one that took a central track. Furthermore, the lateral moisture flux at the boundary of the basin was largely confined to the lowest 4 km above the surface.

4.5. *Regional budgets*

We computed the different components of the water vapour budget (excluding the microphysical forcing) over the four quadrants and present the results in Tables 2–4. The governing equation is

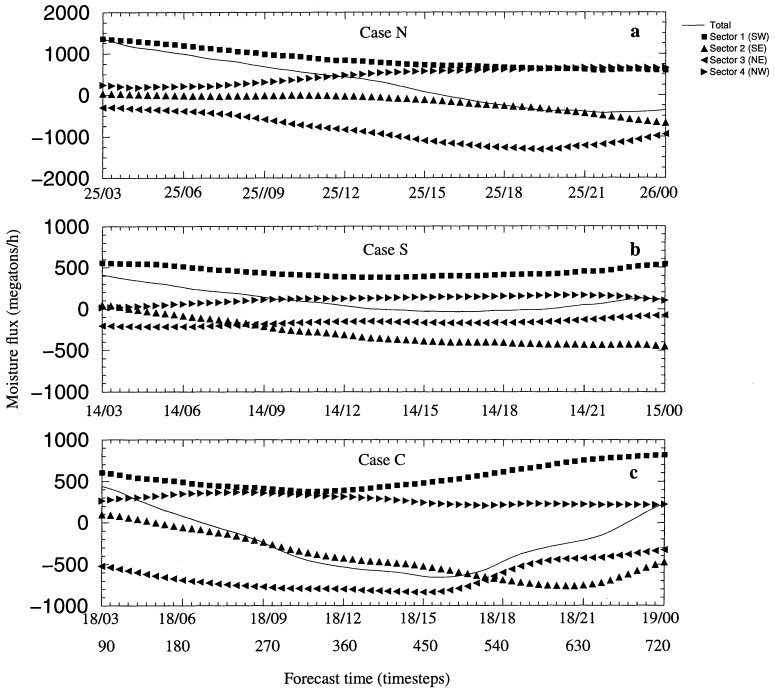

Fig. 10. The net moisture flux through the four sectors for (a) case N, (b) case S and (c) case C. The abscissa denotes the time steps and the corresponding date and time in UTC. The ordinate denotes the magnitude of the flux in units of megatons/h.

similar to (5) except that the area of the MRB is replaced by the area of the appropriate quadrant. The terms are also integrated in time from 03 to 24 h of the simulation.

In case N, the total precipitation in the SW and SE quadrants is less than the corresponding evaporation, while total precipitation far exceeds surface evaporation in the NE and NW quadrants. Unlike the other three quadrants, a net divergence of moisture occurs in the SW quadrant despite large influx of moisture through the SW sector, suggesting that a significant amount of moisture must be transported into the neighbouring SE and NW quadrants.

In case S (Table 3) total precipitation exceeds surface evaporation except in the NW quadrant. This quadrant is also the only one which yields a local moisture surplus with a large net convergence of moisture flux.

Similar to case N, total precipitation is larger than (less than) surface evaporation in quadrants NE and NW (SW and SE) in case C (Table 4). However, in contrast to the previous two cases, this simulation displayed a net divergence of moisture flux in all quadrants except for the NW and a large moisture deficit over the basin results.

In summary, the regional budgets computed over the four quadrants indicate significant variations in sign and magnitude of the storage, net horizontal convergence of moisture, surface evaporation and precipitation terms with the location of the lee cyclone. The total water vapor balance is dominated by net horizontal convergence of water vapor, which determines the sign of the storage term in all three cases. In cases N and S, the convergence is positive and yields a positive storage for water vapor. The latter is, however, smaller than the net convergence because precipitation exceeds evaporation. In case C, net divergence and loss of water vapor are similar, because precipitation is close to evaporation.

4.6. *Rôle of microphysics*

We shall confine our presentation to case N as the dominant microphysical forcing mechanisms

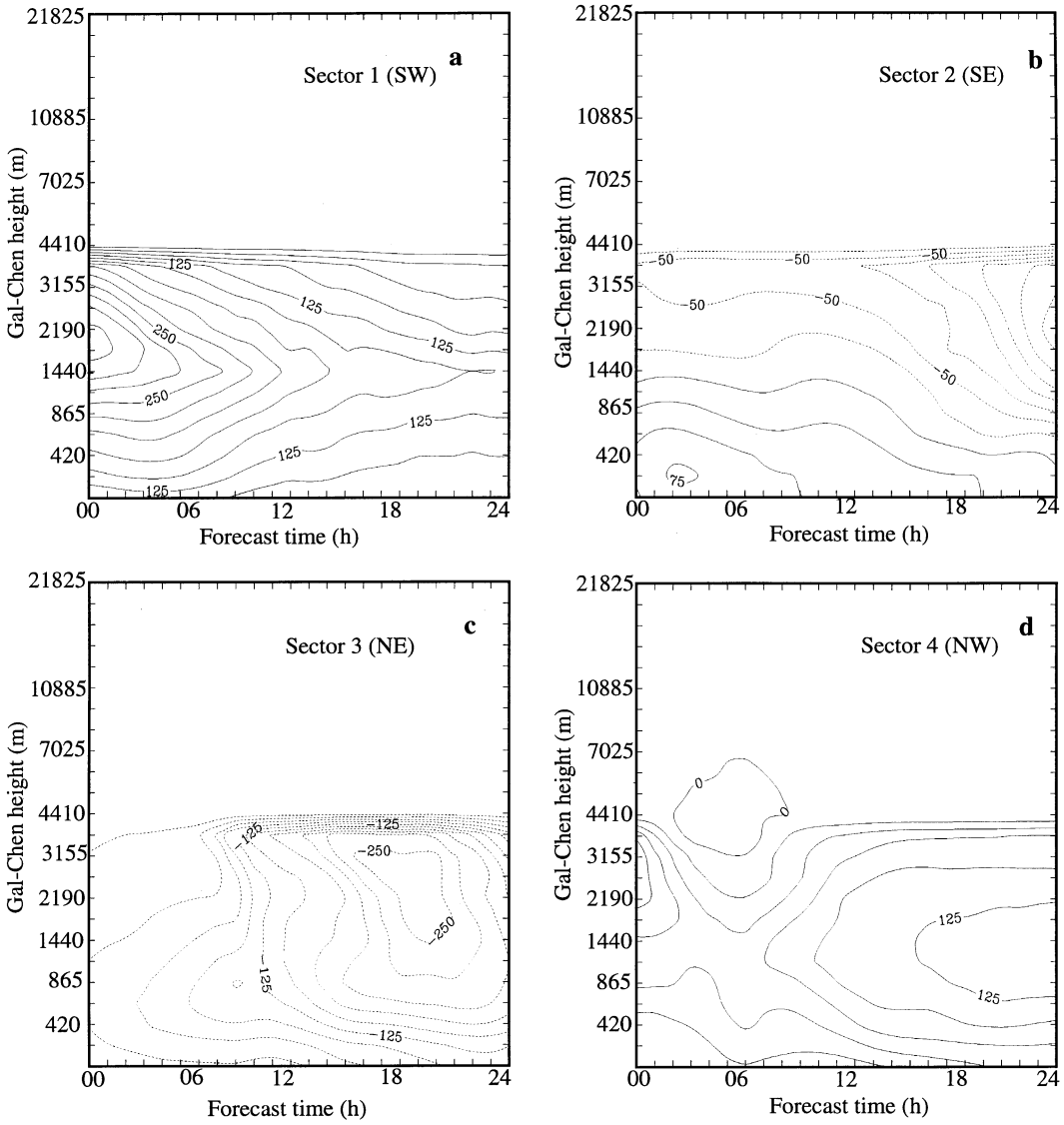

Fig. 11. The time height cross-section of the lateral moisture flux in the basin through (a) Sector 1 (SW), (b) Sector 2 (SE), (c) Sector 3 (NE) and (d) Sector 4 (NW) for case N. The interval is 25 megatons/h. The ordinate represents the height of the Gal-Chen level above the surface (m). The fluxes are multiplied by the factor ($\Delta P g^{-1}$), where ΔP is the pressure interval between successive Gal-Chen levels.

in all three cases exhibit similar behavior. The budgets for q_c, q_r, and q_i are presented in Figs. 12, 13 and 14, respectively. The terms associated with q_g were very small because of weak vertical motion and low rain water content in the basin. It should also be pointed out that graupel is usually associated with deep moist convection which cannot be resolved adequately at a resolution of 18 km.

Fig. 12 indicates that cloud condensation (cloud cond), cloud evaporation (cloud evap), accretion of cloud water by ice (ACLci), and autoconversion and accretion of cloud water to rain water (ACw) essentially determine the storage of the cloud

Table 2. *Components of the vapor budget for case N (megatons)*

	Net horiz. flux conv.	Total precip. (P)	Surface evap. (E)	(P-E)	Storage of q_v
quad 1 (SW)	−6709	1263	2447	−1184	−4979
quad 2 (SE)	5971	1469	1987	−518	6118
quad 3 (NE)	8700	3360	908	2452	5105
quad 4 (NW)	3136	3906	1685	2221	1168
total	11098	9998	7027	2971	7412

Table 3. *Components of the vapor budget for case S (megatons)*

	Net horiz. flux conv.	Total precip. (P)	Surface evap. (E)	(P-E)	Storage of q_v
quad 1 (SW)	−1432	1360	1212	148	−1459
quad 2 (SE)	216	3665	2025	1640	−1595
quad 3 (NE)	−139	1766	755	1011	−1190
quad 4 (NW)	5364	875	1169	−294	5678
total	4009	7666	5161	2505	1420

Table 4. *Components of the vapor budget for case C (megatons)*

	Net horiz. flux conv.	Total precip. (P)	Surface evap. (E)	(P-E)	Storage of q_v
quad 1 (SW)	−446	870	1112	−242	47
quad 2 (SE)	−6407	303	1310	−1007	−5595
quad 3 (NE)	−4220	1412	918	494	−5498
quad 4 (NW)	377	2194	1711	483	117
total	−10696	4779	5051	−272	−10929

Table 5. *Total water budget over MRB for case N (megatons)*

	Net horiz. flux conv.	Surface evap.	Micro. forcing	Total precipitation	Storage term
q_v	11098	7027	−5936	−4777	7412
q_c	172		−144		28
q_r	−63		4714	−4671	−20
q_i	−1086		1358	−542	−270
q_g	0		8	−8	0
total	10121	7027	0	−9998	7150

water (tend. of q_c) in the basin. The rain water budget in Fig. 13 illustrates that the storage of rain water (tend. of q_r) in the MRB is balanced primarily by the melting of ice to rain (AMLir), sedimentation (Sedimentation) of rain water (which forms part of the stratiform precipitation at the surface), evaporation of rain water (rain evap) and autoconversion and accretion of cloud water to rain (ACw). In the ice budget (Fig. 14), the major sources are deposition (AVDvi) and the accretion of cloud water by ice (ACLci). The major sinks include melting of ice to rain (AMLir), the horizontal flux divergence of ice (negative conv. hor. flux) and during the latter part of the integration, sedimentation of ice (sedimentation). Most striking from these budgets is that the

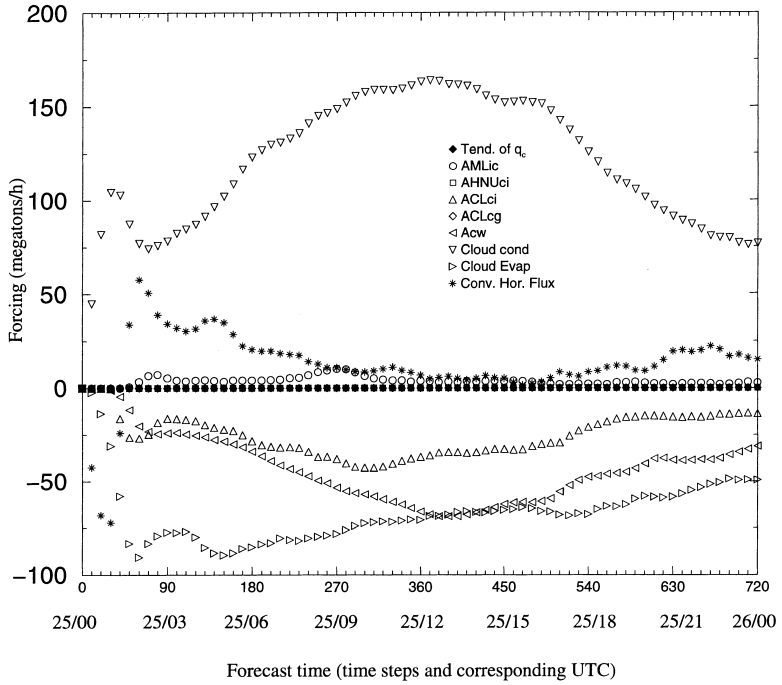

Fig. 12. Same as Fig. 5 but for cloud water.

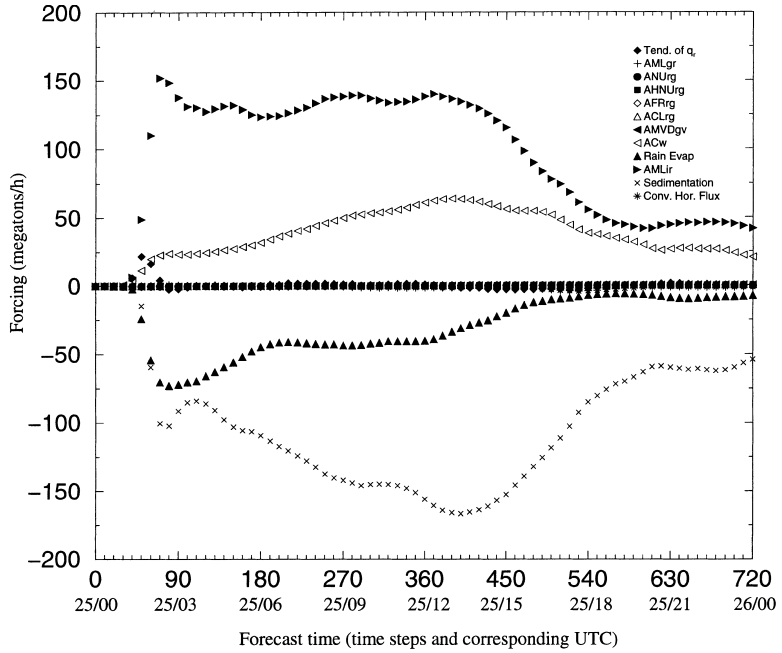

Fig. 13. Same as Fig. 5 but for rain water.

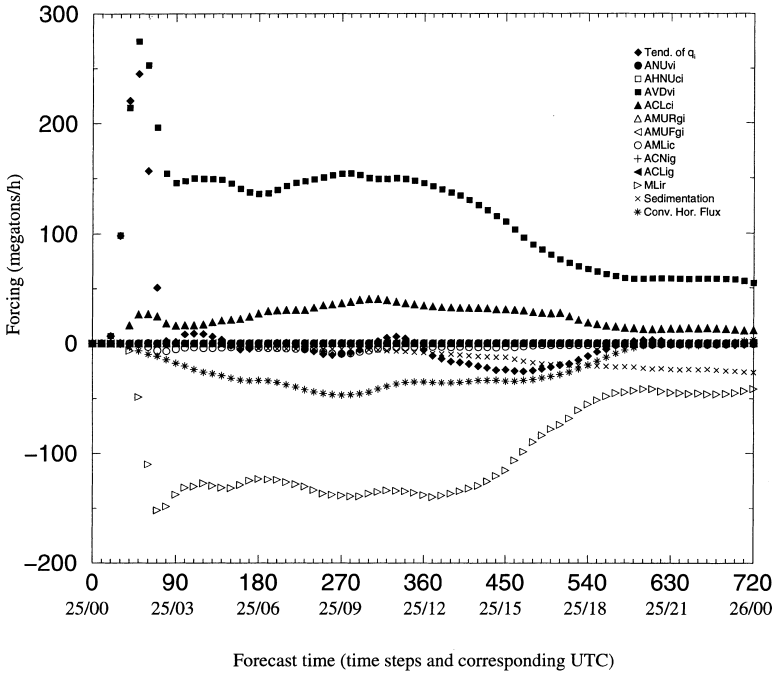

Fig. 14. Same as Fig. 5 but for ice.

Table 6. *Total water budget over MRB for case S (megatons)*

	Net horiz. flux conv.	Surface evap.	Micro. forcing	Total precipitation	Storage term
q_v	4009	5161	−2401	−5349	1420
q_c	−98		127		29
q_r	−18		2294	−2290	−14
q_i	−36		−21	−26	−83
q_g	0		1	−1	0
total	3857	5161	0	−7666	1352

Table 7. *Total water budget over MRB for case C (megatons)*

	Net horiz. flux conv.	Surface evap.	Micro. forcing	Total precipitation	Storage term
q_v	−10696	5051	−2507	−2777	−10929
q_c	−333		455		122
q_r	−8		1893	−1888	−3
q_i	117		157	−112	162
q_g	0		2	−2	0
total	−10920	5051	0	−4779	−10648

tendencies of q_c, q_r, and q_i averaged over the whole basin are very small relative to their forcing. Thus, there is a critical balance amongst the source and sink terms. Furthermore, the magnitudes of the flux convergence of these water species appear small relative to the largest microphysical forcing terms.

Figs. 15a–c, 16a–c and 17a,b show the time

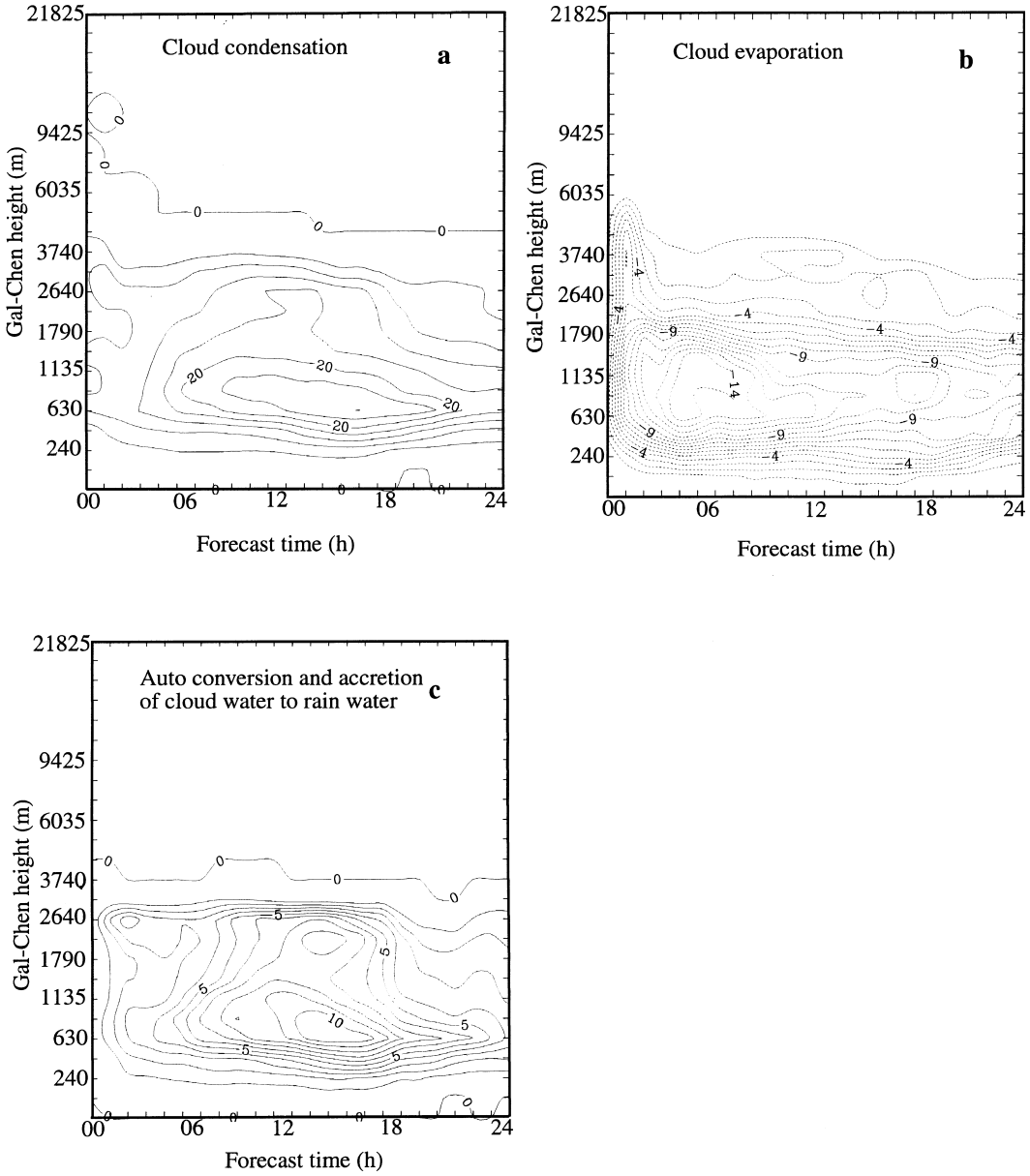

Fig. 15. The time height cross-section of (a) Cloud condensation (Int.: 4 $gm^{-2}\ h^{-1}$), (b) Cloud evaporation (Int.: 1 $gm^{-2}\ h^{-1}$) and (c) Auto-conversion and accretion of cloud water to rain water (Int.: 1 $gm^{-2}\ h^{-1}$). The ordinate represents the height of Gal-Chen level (m). The terms are multiplied by the factor ($\Delta P g^{-1}$), where ΔP is the pressure interval between successive Gal-Chen levels.

height plot of cloud condensation, cloud evaporation, auto-conversion and accretion of cloud water by rain drops, sedimentation of rain water, evaporation of rain water, melting of ice to rain, net deposition and accretion of cloud water by ice respectively. These quantities represent averages over the horizontal area of the MRB. Cloud condensation (Fig. 15a) shows maximum values

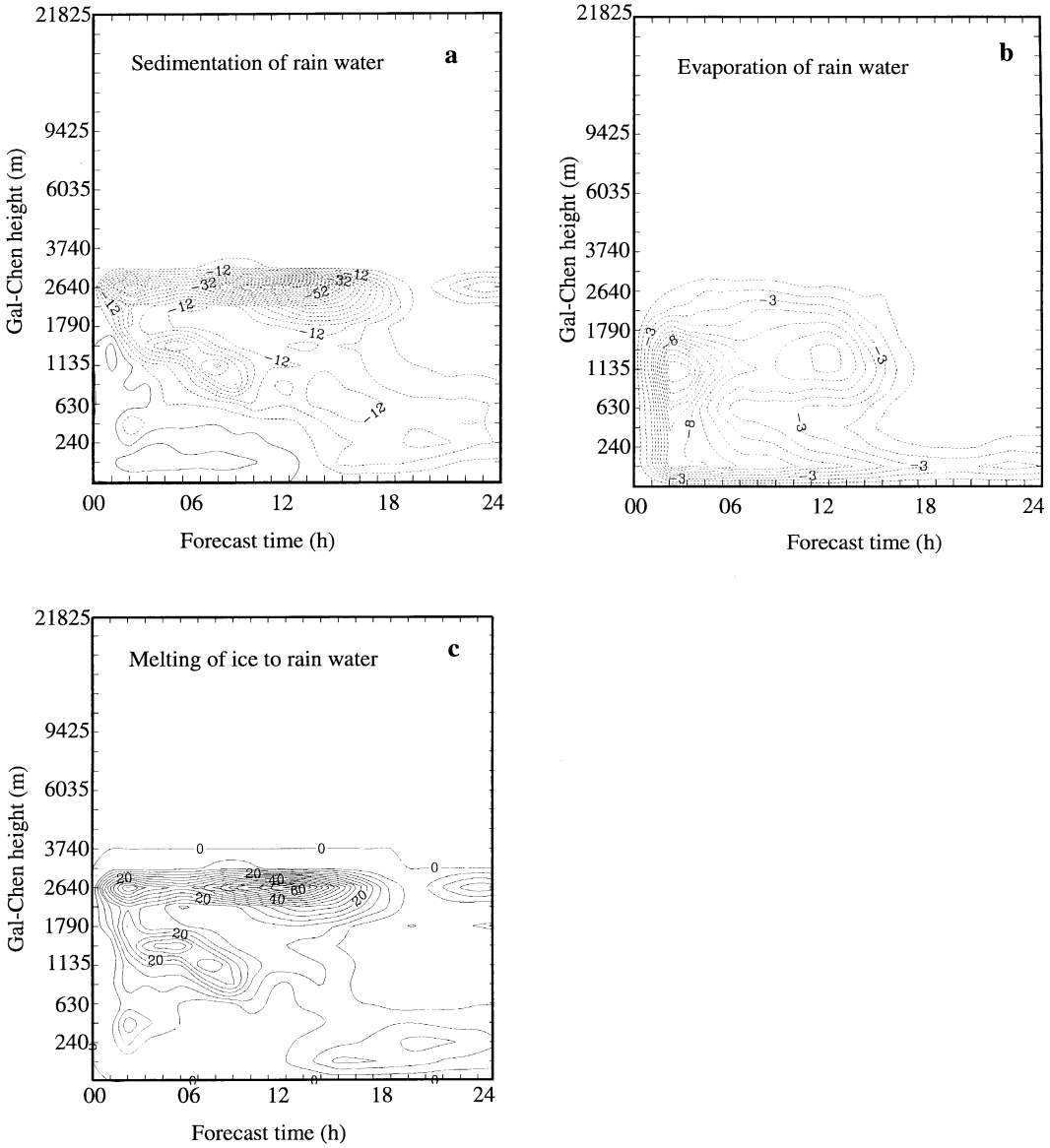

Fig. 16. Same as Fig. 15 but for (a) Sedimentation of rain water (Int.: 4 $gm^{-2}\ h^{-1}$), (b) Evaporation of rain water (Int.: 1 $gm^{-2}\ h^{-1}$) and (c) Melting of ice to rain water (Int.: 4 $gm^{-2}\ h^{-1}$).

in a layer between 630 m and 1135 m above the surface from 6 to 18 h of the integration. This corresponds well with the maxima in accretion and autoconversion of cloud water to rain water (Fig. 15c) and the location of a large amount of evaporation (Fig 15b). Melting of ice to rain (Fig. 16c) contributes significantly to sedimentation (Fig. 16a) and evaporation of rain water (Figs. 16b). Net deposition (Fig. 17a) occurs in altitude from around 3155 m to 10885 m. Net sublimation is however very small implying that on average, the air over the basin is saturated with respect to ice in a very deep layer above the ground. The accretion of cloud water by ice (Fig. 17b), the

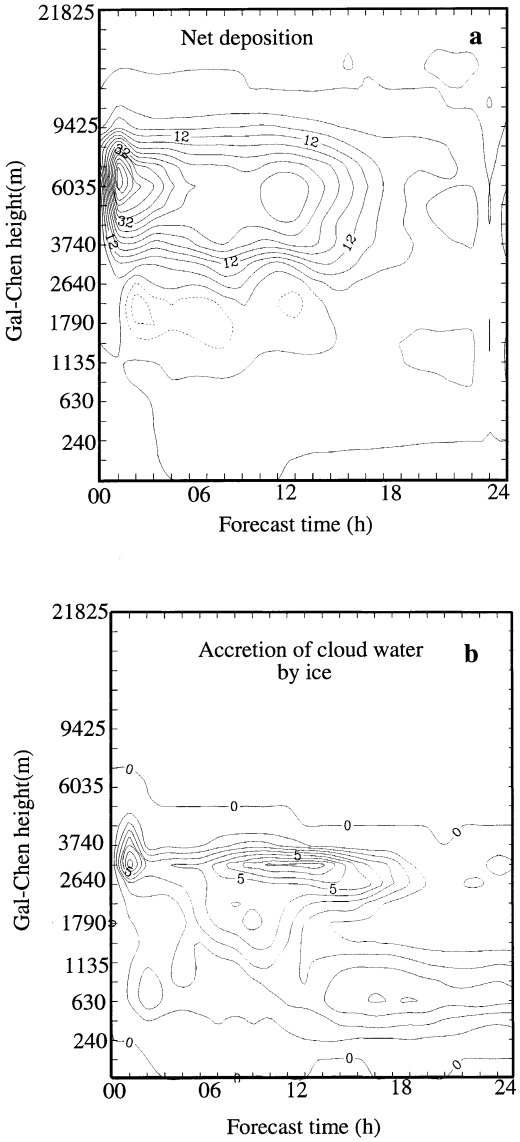

Fig. 17. Same as Fig. 15 but for (a) Net deposition of water vapor to ice crystals (Int.: 4 $gm^{-2}\ h^{-1}$) and (b) Accretion of cloud water by ice (Int.: 1 $gm^{-2}\ h^{-1}$).

other major source of ice in the simulation, appears in the lower troposphere below 3740 m where cloud water is prevalent.

5. Conclusions

The objective of this study is to determine the total water budget during the formation and passage of lee cyclones over the Mackenzie River Basin (MRB). Three lee cyclogenesis events that occurred in the northern, central and southern parts of the basin were simulated using a non-hydrostatic mesoscale model with explicit microphysics at a resolution of 18 km. The source and sink terms of water vapor (q_v), cloud water (q_c), rain water (q_r), ice (q_i) and graupel (q_g) were then analyzed. This type of modeling strategy is particularly useful given the low density of observations over the MRB.

Tables 5–7 summarize the budgets of the water species including the storage term, the net horizontal flux convergence, the total microphysical forcing (all the microphysical terms), total precipitation, and surface evaporation from 03 to 24 h of the integration. Note that precipitation is preceded by a negative sign here because it acts as a sink to the corresponding water species. The results indicate that the net horizontal moisture flux convergence into the basin plays a decisive role in the overall water budget. In all three cases, it explains qualitatively the change in the total storage term, which is strongly dominated by the storage of water vapor. In cases N and S, the convergence of moisture flux is positive and gives a positive change in storage. The storage is, however, smaller than the net convergence because precipitation exceeds evaporation. In case C, net divergence and loss of water are similar, because precipitation is close to evaporation. Furthermore, the cyclones which formed at the northern and the southern extremity of the basin resulted in a net gain of basin moisture while the cyclone which traversed the central portion of the MRB resulted in a net loss. The regional budgets calculated over four separate quadrants indicated large local variations in all three cases.

Deposition, condensation, melting of ice to rain, autoconversion and accretion of cloud water by rain drops, accretion of cloud water by ice and evaporation of rain and cloud water were the dominant microphysical processes involving different water species. The flux convergences of q_c, q_r, q_i and q_g were much smaller than some of the microphysical generation terms. The local tendencies of all water species except for q_v were much smaller than their forcing indicating the existence of a strong and intricate interrelationship between the source and sink terms.

We recognize that only 3 cases were examined.

Some of the results, especially the drying of the basin for the centrally tracking storm, may vary from case to case. The study of more events is needed to confirm the general validity of the findings presented in this paper.

6. Acknowledgements

This research was supported by the National Science and Engineering Research Council of Canada under a GEWEX collaborative research network grant. The authors thank the reviewers for constructive comments which led to substantial improvement in the manuscript.

7. Appendix

List of symbols

Symbol	Description
ACLcg	accretion of cloud water by graupel
ACLci	accretion of cloud water by ice
ACLig	accretion of ice by graupel
ACLrg	accretion of rain water by graupel
ACNig.	autoconversion of ice to graupel
ACw	accretion of cloud water by rain and auto conversion of cloud water
AFRrg	contact freezing of rain water to graupel
AHNUci	homogeneous nucleation of cloud water to ice at temperatures below -40°C
AHNUrg	homogeneous nucleation of rain water to graupel at temperatures below -40°C
AMLic	melting of ice to cloud water
AMLir	melting of ice to rain water
AMLgr	melting of graupel to rain water
AMUFgi	ice multiplication during freezing of rain drops
AMURgi	ice multiplication during riming of ice and graupel particles
AMVDgv	evaporation of melting graupel particles
ANUrg	heterogeneous (immersion) freezing of rain water to graupel
ANUvi	nucleation of ice from vapour
AVDgv	net sublimation of graupel to vapor
AVDvi	net deposition of water vapor to ice crystals
CD	convective drying
CE	cloud evaporation
Cond.	cloud condensation
D	vertical divergence of turbulent moisture flux
RE	evaporation of rain water
SQg	sedimentation of graupel
SQi	sedimentation of ice
SQr	sedimentation of rain water

REFERENCES

Benoit, R., Cote, J. and Mailhot, J. 1989. Inclusion of a TKE boundary layer parameterization in the Canadian regional finite element model. *Mon. Wea. Rev.* **117**, 1726–1750.

Benoit, R., Desgagne, M., Pellerin, P., Pellerin, S., Chartier, Y. and Desjardins, S. 1997. The Canadian MC2: a semi-Lagrangian, semi-implicit wideband atmospheric model suited for finescale process studies and simulation. *Mon. Wea. Rev.* **125**, 2382–2415.

Bjornsson, H., Mysak, L. A. and Brown, R. D. 1995. On the interannual variability of precipitation and runoff in the Mackenzie drainage basin. *Climate Dyn.* **12**, 67–76.

Deardorff, J. W. 1978. Efficient prediction of ground surface temperature and moisture with inclusion of a layer of vegetation. *J. Geophy. Res.* **83**, 1889–1903.

Garand, L. and Mailhot, J. 1990. The influence of infrared radiation on numerical weather forecasts. *Preprints, 7th Conf. on Atmospheric radiation*, San Francisco, Ca, Amer. Meteor. Soc., J146–J151.

Kong, F.-Y. and Yau, M. K. 1997. An explicit approach to microphysics in MC2. *.Atmos.-Ocean.* **35**, 257–291.

Kong, F.-Y., Huang, M.-Y. and Xu, H.-Y. 1990. 3-dimensional numerical simulations of ice-phase microphysical in cumulus clouds. Model establishment and ice-phase processes parameterization. *Chinese J. Atmos. Sci.* **14**, 437–450.

Krishnamurti, T. N., Bedi, H. S., Oosterhof, D. K. and Rohaly, G. D. 1996a. Atmospheric moisture budget during a Bangladesh flood event. *Int. J. Clim.* **16**, 791–803.

Krishnamurti, T. N., Bedi, H. S., Rohaly, G. D. and Oosterhof, D. 1996b. Partitioning of the seasonal simulation of a monsoon climate. *Mon. Wea. Rev.* **124**, 1499–1519.

Lackmann, G. M. and Gyakum, J. R. 1996. The synoptic and planetary-scale signatures of precipitating systems over the Mackenzie River Basin. *Atmos.-Ocean.* **34**, 647–674.

Lackmann, G. M., Gyakum, J. R. and Benoit, R. 1998. Moisture transport diagnosis of a winter precipitation event in the Mackenzie River Basin. *Mon. Wea. Rev.* **126**, 668–691.

Mailhot, J. and Chouinard, C. 1989. Numerical forecasts of explosive winter storms: Sensitivity experiments with a meso-α model. *Mon. Wea. Rev.* **117**, 1311–1343.

Smirnov, V. V. and Moore, G. W. K. 1999. Spatial and temporal structure of atmospheric water vapor transport in the Mackenzie River Basin. *J. Climate* **12**, 681–696.

Walsh, J. E., Zhou, X., Portis, D. and Serreze, M. C. 1994. Atmospheric contribution to hydrologic variations in the arctic. *Atmos.-Ocean.* **32**, 733–755.